

## “OBSERVING AND ANALYZING” IMAGES FROM A SIMULATED HIGH REDSHIFT UNIVERSE

ROBERT J. MORGAN, ROGIER A. WINDHORST, EVAN SCANNAPIECO  
School of Earth and Space Exploration, Arizona State University, Tempe, AZ 85281-1406

AND ROBERT J. THACKER  
Dept. of Physics and Astronomy, St. Mary’s University, Halifax, NS B3H 3C3, Canada  
*Draft version March 3, 2024*

### ABSTRACT

We investigate the high-redshift evolution of the restframe UV–luminosity function (LF) of galaxies via hydrodynamical cosmological simulations, coupled with an emulated observational astronomy pipeline that provides a direct comparison with observations. We do this by creating mock images and synthetic galaxy catalogs of  $\approx 100$  arcmin<sup>2</sup> fields from the numerical model at redshifts  $\approx 4.5$  to 10.4. We include the effects of dust extinction and the point spread function (PSF) for the Hubble WFC3 camera for comparison with space observations. We also include the expected zodiacal background to predict its effect on space observations, including future missions such as the James Webb Space Telescope (JWST). When our model catalogs are fitted to Schechter function parameters, we predict that the faint-end slope ( $\alpha$ ) of the LF evolves as  $\alpha = -1.16 - 0.12 z$  over the redshift range  $z \approx 4.5$  to 7.7, in excellent agreement with observations from e.g., Hathi et al. (2010). However, for redshifts  $z \approx 6$  to 10.4,  $\alpha(z)$  appears to display a shallower evolution,  $\alpha = -1.79 - 0.03 z$ . Augmenting the simulations with more detailed physics — specifically stellar winds and supernovae (SN) — produces similar results. The model shows an overproduction of galaxies, especially at faint magnitudes, compared with the observations, although the discrepancy is reduced when dust extinction is taken into account.

*Keywords:* galaxies: luminosity function; galaxies: hierarchical simulations

### 1. INTRODUCTION

The luminosity function (LF) of galaxies is an important indicator of galaxy assembly and evolution (Schechter, 1976). It traces the star-formation rate (SFR) and contains clues to physical processes such as galaxy merger rates, and also feedback from supernovae (SN) and active galactic nuclei (AGN). Numerical simulations are essential to understanding and predicting the highly non-linear processes in large scale structure formation, but are often difficult to interpret with respect to the actual astronomical observations. This is due to many factors, such as the presence of detector noise and the sky-background. It is thus non-trivial to draw precise inferences from a comparison between numerical predictions and the images actually observed in astronomy. Overzier et al. (2013) characterized the current state of the relation between theory and observation as being mostly one-directional, in that “physical quantities estimated from observations were compared with theoretical predictions,” and that a greater understanding could be gained by going in the other direction.

To help bridge this gap between theory and observations, we extend the numerical models to include the simulation of an observational pipeline. That is, we form “artificial” images from the simulations of galaxy formation, using the stellar population synthesis models of Bruzual & Charlot (2003, hereafter BC03) to predict the observed stellar light distribution, and process these to create mock galaxy catalogs using Source Extractor (“SExtractor”; Bertin & Arnouts 1996) after imposing the appropriate amount of image noise due to the zodiacal background.

Overzier et al. (2013) summarized previous work done

in this area, such as Bouwens et al. (1999), who coupled galaxy evolution models to spectral energy distribution (SED) models to predict luminosities at high redshifts, and Bouwens, Illingworth & Magee (2006), who predicted the evolution of galaxy properties by artificially redshifting selected galaxy images, producing new synthetic images. They also discuss producing “observed” image sets from semi-analytic models (SAMs).

Realistic synthetic telescope images produced from the output of hierarchical simulations to emulate sky surveys were generated by e.g., Blaizot et al. (2005). Synthetic observations are also produced using the output of SAMs by processing the results of DM halo simulations. They used methods similar to those used here, in terms of the use of translation and rotation of multiple slices of data at different redshifts to produce artificial images and catalogs.

There have also been many numerical simulations of galaxies without producing mock observations, mostly with SAMs (e.g., Bolton & Haehnelt 2007; Mao et al. 2007; Samui et al. 2009; Trenti et al. 2010; Dayal et al. 2014), as well as Overzier et al (2013). Dayal et al. (2014) used models of star-formation and merger trees of DM haloes to simulate properties of high redshift galaxies. Hydrodynamical simulations with dark matter (DM), gas and stars have been used to study galaxies (e.g., Jonsson et al. 2006; Lotz et al. 2008, 2010; Robertson & Bullock 2008; Wuyts et al. 2009; and Chilingarian et al. 2010). However, these were mainly used to study the effects of dust on the observations, and were not on cosmological scales. Relatively recently, there have been hydrodynamical simulations, investigating the galactic LF at high redshift (e.g., Nagamine et al. 2006; Finlator, Davé,

& Oppenheimer 2007; Salvaterra, Ferrara & Dayal 2011; Gabor & Davé 2012, Jaacks et al. 2012; Stinson et al. 2013; Shimizu et al. 2014).

Jaacks et al. (2012) included star-formation, dust extinction plus IGM transmission effects. They calculated the SED of each selected galaxy using BC03 to make spectrophotometric comparisons with the observations. They also ran different simulations at different resolution scales to cover the bright, medium and faint-end of the LF scale, and then combined the results. We discuss this later in §5.4.

Salvaterra et al. (2011) have also studied the high redshift galactic LF. Shimizu et al. (2014) performed large hydrodynamical simulations with both DM and baryonic matter including star-formation, SN feedback, and feedback winds. They calculated the SEDs of each star particle and included dust attenuation, and created mock observations in order to make comparisons with the observed UDF12 field. We discuss the results of these groups later in §6, when discussing our own results.

In this work, we use gas and hydrodynamic models based on the Gadget2 code (Springel (2000); Springel et al. 2001; Springel & Hernquist 2003), including star-formation, to avoid many of the assumptions necessarily made in SAM approaches. The use of hydrodynamic numerical simulations limits our ability to reproduce survey-size scales of many square degrees over cosmological time scales. However, we are able to produce images on the scales of the Great Observatories Origins Deep Surveys (GOODS) mosaics fields of 8 – 10 arcminutes with HST, and in the future also with JWST, at redshifts of  $z \simeq 4.5$  to 11. It is time-consuming to run hydrodynamical simulations with different sets of parameter values. Hence, it is crucial to perform these simulations with minimal assumptions, to see how well we can reproduce the actual observations with physics-based model inputs. This also aids in deducing the possible effects of different physics on the outcome, as these can be added to the model. This was also done by Haas (2010), who used hydrodynamic simulations from the Overwhelmingly Large Simulations (Schaye et al. 2010) to study the LFs of mock galaxies, though this work was in the  $K$ - and  $B$ - band filters and confined to lower redshifts,  $z < 4$ .

Overzier et al. (2013) pursued a similar approach in the “Millennium Run Observatory” (MRObs), using semi-analytical models. They implemented a rich user-interface for perusing the simulation data-base at different wavelengths and filters, and included a number of observational artifacts. Our work is more focussed on predicting the faint-end of the luminosity function (LF) of galaxies, something that is of considerable interest to observers and relevant to the direct planning of missions such as JWST. The results presented here can thus potentially be used to guide the planning of future JWST observations.

## 2. METHODOLOGY

### 2.1. Summary of Method

Numerical simulations are used to predict synthetic images similar to those that may be observed at high redshifts (§2.2). Our simulation code is a variant of Gadget2 (Springel 2005) that includes additional physics modules,

such as star-formation and feedback from supernovae as well as radiative cooling processes.

Since our intent was not to create an exact simulation of any particular instrument — but rather to include the most important and general observational artifacts, including adding the effects from dust — some simplifications were made. The photon energy is considered to be solely from the simulated stellar populations, without significant reprocessing. Hence, in our first analysis we do not consider extinction by dust, although we discuss its effects later (§3.6). There is also no attempt to include artifacts such as confusion from foreground galaxies, whether from natural overlap (Windhorst et al. 2008) or gravitational lensing (Wyithe et al. 2011). Note that confusion from foreground stars can be safely ignored, as the faint star-counts have a much flatter slope than the faint galaxy counts in the red-near-IR (e.g., Windhorst et al. 2011).

Simulation outputs at various redshifts include stellar particles that model the star-formation and evolution in the simulation, as explained in §3.1. We treat these particles as simple stellar populations (SSPs) with a given age and metallicity, as determined in the model. For these, spectral energy distributions (SEDs) in the emitted rest-frame are derived using the BC03 models (§3.2). Fluxes are calculated in the simulated observer’s frame, integrated with filter response functions (§3.3), and converted to images (§3.1) in the FITS (Greisen et al. 1980) format (§3.4). As explained in §3.1, the size of each frame in pixels is determined from the relative comoving distance in our adopted  $\Lambda$ CDM cosmology. This permits “stacking” of frames at different redshifts.

We assume WMAP values available at the time of the simulation,  $H_0 = 71.9$ ,  $\Omega_\Lambda = 0.742$ , and  $\Omega_b = 0.0441$ , (Komatsu et al. 2009). A slightly different value (0.73) for  $\Omega_\Lambda$  was used for the calculation of distances, due to more recent WMAP7 values (Komatsu et al. 2011). However, this does not affect the restframe absolute magnitude calculation, since the same luminosity distance was used in calculating the flux in the observer’s rest-frame. Since the simulations were run, more recent values have become available from Planck (2015), but as our values are within  $\sim 5\%$  of those, this shouldn’t make much of a difference, since the *simulated physical* parameters are likely uncertain by at least this much.

The method of projecting the 3-D data onto the 2-D sky-plane is described in §3.1. These images are analyzed by the SExtractor package (Bertin & Arnouts 1996) to find “SF-particle” close groupings (see Fig. 1), that are treated as ‘galaxies’ or ‘galaxy building blocks’, and binned into observed magnitude ranges. This process is then repeated, adding effects from dust extinction and PSF-convolution (§3.6).

The luminosity functions (LFs) are fitted to a Schechter (1976) function, and best-fit estimates of the faint-end LF slope parameters  $\alpha$ , characteristic magnitude  $M^*$ , and the density normalization  $\phi^*$  are found using chi-square minimization (§4). Contours of chi-square in the  $\alpha - M^*$  plane for best-fit normalizations, as well as the LF slope  $\alpha$ , are presented in §5 as a function of redshift and compared with the observations from Hathi et al. (2010).

We repeat the analysis for different model parameters intended to include effects from stellar and galactic

winds. Also, the appropriate amount of simulated ‘sky-noise’ (foreground zodiacal light; for a summary, see Table 2 of Windhorst, et al. 2011) is added to the images to simulate deep-space environments, and the image extraction and data reduction process is repeated to evaluate the effect of these noise sources on the “observation” of the underlying SPH model. This process is also repeated for adding effects from dust extinction and PSF convolution (§3.6).

We note that this use of SExtractor is a departure from the usual method of treating simulated galaxy data, but not actual observed galaxy images. The intent of this work is to create “mock observations” using “mock galaxy images”. To check this use of SExtractor, a comparison was made with a publicly available “friend-of-friends” (“FOF”) tool from the U. of Washington Dept. of Astronomy <sup>1</sup>, which is a more usual method of extracting groupings from this type of simulated data. We found a 96.9 percent correlation between the number of groups found using the two methods on the same simulated frame. Specifically, using a 20 Kpc “linking length” parameter on a snapshot at redshift 7.3, “FOF” found 8987 groups, while SExtractor found 8711 objects. We attribute the discrepancy to SExtractor’s requirement that pixels with flux above the threshold be contiguous in order to be considered an object. This agreement is sufficiently good to proceed with the method.

## 2.2. Details of the Numerical Simulation

The numerical simulations include both dark matter and gas particles. Besides simulating the effects of gravity, it uses smoothed particle hydrodynamics (SPH), (Gingold & Monaghan 1977; Lucy 1977), heating and cooling (Katz et al. 1996), and star-formation (Springel & Hernquist 2003, hereafter SH03). A hybrid gas/star-particle model is employed, which has both cool and hot gas, and stellar components for sub-grid modeling. Star ‘particles’ are formed from the hybrid gas-particles, representing a stellar population or star-cluster, when 50% of the hybrid particle has been converted to stars.

While the exact details of the star-formation procedure are complex (see SH03 for a detailed description), the rate of production of stars is essentially determined by the density of cold gas clouds divided by the characteristic timescale of star-formation,  $\tau$ . An external UV-background, based upon a modified Haardt & Madau (1996) spectrum is also included (see Davé et al. 1999 for details). This background turns on at  $z \approx 6$  and is included in the calculation of ionization state abundances of H and He, which determines the net cooling rate and thus impacts the formation of cold clouds.

The simulation volume was a cube 18 comoving Mpc/h on a side, ( $h = H_0/100 \text{ km sec}^{-1} \text{ Mpc}^{-1}$ ), with periodic boundary conditions, using  $2 \times 512^3$  particles, with equal numbers of dark matter and gas particles, yielding a baryon-mass resolution of  $5.4 \times 10^5 h^{-1} M_\odot$  per particle.

Initial conditions were generated using 2nd order Lagrangian perturbation theory (e.g., Thacker & Couchman 2006) at an initial redshift of  $z = 199$ . Model outputs of particle data were recorded at time intervals corresponding to two light crossing times of the simulation

cube, where a light crossing time is the time it takes light to travel from one side to the opposite side, ignoring the small expansion of space in this time. Thus, the light crossing time is given by  $18 \text{ Mpc } h^{-1} (1+z)^{-1} \text{ c}^{-1}$ . The star-formation code creates stars in the multi-phase gas particles when a sufficient fraction of the gas reaches appropriate temperature and density conditions (SH03). When 50% of the hybrid particle mass is processed into stars, that portion is split off as a “star-particle.” These star-particles have masses  $2.7 \times 10^5 h^{-1} M_\odot$ , or roughly a globular cluster or Giant Molecular Cloud (GMC) mass. The particle files were processed to extract data on the star-particles, including mass, metallicity and formation time, which were used to obtain rest-frame SEDs from the BC03 models. In later runs, parameters were set to permit the simulation of feedback via galactic winds, largely from simulated supernovae, and shocks and heating of the gas from the SNe and star-formation. These runs are described as including ‘winds’ in the text and figures. See Table 1 for parameter values, which were taken from SH03.

**Table 1**  
Cosmological and Physical Simulation Parameters Used.

Parameter	Value
OmegaLambda ( $\Omega_\Lambda$ )	0.742
OmegaBaryon ( $\Omega_B$ )	0.0441
HubbleParam (h)	0.719
Softening Length	$1.8 h^{-1} \text{ kpc}$
‘Winds’ Parameters	
WindEfficiency	0.5
WindEnergyFraction	0.25
WindFreeTravelLength	0.5

Parameters used in simulations *without* feedback “winds” and *with*. Names used are the parameter names in the model, except for ‘Softening Length’, which is the gravitational softening length and the SPH kernel size. Feedback ‘Wind’ parameter values were taken from SH03. Lengths are in comoving units.

**Table 2**  
Simulated SExtractor Object Counts.

Redshift	No BG	Sky BG	Recovered Fraction	Number of Snapshots
4.52	15334	2407	0.157	1
5.32	13809	2140	0.155	1
6.01	13392	1986	0.148	1
6.24	49818	7235	0.145	5
7.16	39766	3223	0.081	5
7.68	36213	3248	0.090	5
10.38	12702	967	0.076	5

Recovered Object fraction “with” compared to “without” sky background (BG). SExtractor counts of the same synthetic galaxy fields at different redshifts without added sky BG, and with added sky BG  $\approx 22.6 \text{ AB-mag arcsec}^{-2}$ . At redshifts  $z \geq 6.24$ , five (5) snapshots are combined, while at  $z < 6.24$  only a single snapshot is used, hence the increase in counts. For details, see text. We note a sharp decrease in completeness (ratio of counts with sky BG to counts without sky BG) at redshift  $z \geq 7.16$ . We also note a sharp drop in the total counts for redshift  $z > 7.68$ .

<sup>1</sup> <http://www-hpcc.astro.washington.edu/tipsy/top.html>

### 3. IMAGE SYNTHESIS

#### 3.1. Simulated Image and Pixel Scales

The simulated image pixel-scale was chosen to be comparable to the resolution of space-based instruments such as HST and JWST. This scale is also consistent with the size of astrophysical objects most closely represented by the model particles, such as GMCs and massive star-forming regions with masses  $M \leq 10^6 M_\odot$ . That is, the hybrid gas-star particles represent star-forming regions. The pixel-scale of the WFC3 camera on the HST at the near-IR wavelengths simulated here is  $0.13''/\text{pixel}$  (Windhorst et al. 2011.) JWST will have a near-IR pixel scale of  $0.034 - 0.068''$ , with a near-IR image resolution of  $\approx 0.06''$  FWHM (Gardner et al. 2006).

A reference scale was set at redshift  $z = 3.0$  for the FITS frame sizes. For the chosen  $\Lambda$ CDM cosmology, a redshift  $z \simeq 3$  corresponds to a comoving distance of 6.4 Gpc. A sky-field of 18 comoving Mpc/h on a side would then be  $808 \times 808$  arcsecs, roughly the size of GOODS-sized mosaics with HST, and similar future projects that the community will likely propose for JWST. Specifically, the JWST NIRCcam — which covers the range of 0.6 to 5.1 microns — has a field of  $132 \times 264$  arcsecs<sup>2</sup>. A typical mosaic is expected to be  $\approx 3 \times 4$  tiles, or  $\approx 400 \times 500$  arcsecs, which would be of the order of the higher redshift simulated images, since the size scales inversely with the comoving distance.

One of the reasons for doing our simulations is to get better guidance how to best plan searches for First Light objects at  $z \gtrsim 10$ . Currently, the JWST Guaranteed Time Observations (GTO) observations are planned to be a combination of 1–2 deep fields (1–2 $\times$ 100 hrs) to  $AB \lesssim 31$  mag, plus a larger number ( $\sim 10 \times 10$  hrs) of complementary medium-deep fields to  $AB \lesssim 30$  mag. In addition, we anticipate that the JWST GO community may propose for one JWST UltraDeep Field (1 $\times$ 800 hrs) to  $AB \lesssim 32$  mag, and possibly also a set of CANDELS or COSMOS like ultra-wide JWST fields to  $AB \lesssim 29$  mag. Combined, these wedding-cake layered JWST GO and GTO surveys would in the end provide the best combination of depth, dynamic range, area, and sampling of cosmic variance of the LF at  $4 \lesssim z \lesssim 11$  or higher. Our simulations are thus designed to cover at least the observed flux range of  $24 \lesssim AB \lesssim 31$  mag in such JWST surveys.

We chose an image size with a power of 2, to conform to common detection formats. A field of  $8192 \times 8192$  pixels yields a scale of  $0.099''/\text{pixel}$ , which is in between that of Hubble WFC3/IR ( $0.13''/\text{pix}$ ) and JWST NIRCcam ( $0.034$  to  $0.068''/\text{pix}$ ). As the simulation has a fixed volume in comoving space, the simulated frame-sizes are inversely proportional to the comoving distance, which also maintains the pixel angular scale.

While the simulation does not permit pixel-resolution down to actual astrophysical objects with masses less than  $10^5 M_\odot$  — although subgrid methods are used to simulate smaller sizes — this still corresponds roughly to the upper end of GMC and massive star-forming region masses. These have typical sizes of order 50 — 100 pc. At  $z = 4.5$ , 100 pc corresponds to  $0.015''$ , at  $z = 6$ , to  $0.017''$ , and at  $z = 10$ , to about  $0.024''$ . Thus, a  $\sim 10^5 M_\odot$  object at this pixel scale would be sub-pixel

at these distances, even for JWST (note that these are proper sizes here). At redshifts higher than 6.3, the simulated frames were formed by “stacking” five (5) consecutive snapshots, in order to simulate a larger volume of the simulated “observed” space. Table 2 shows the number of snapshots used for each redshift image. To avoid aliasing effects — since the same space was being captured at different lookback times — advantage was taken of the simulation’s periodic boundary conditions. Each frame was rotated in a cyclic permutation about the edges of the data cube before being projected on the sky-plane corresponding to the new  $x - y$  plane. Next, the images were shifted randomly in the sky-plane, applying periodic conditions. These projections were then combined into a single frame. The effective redshift was taken as the median of the contributing frame-redshifts. The size of the merged frames was taken as the minimum (farthest) image frame in the contributing set of that redshift slice.

The total volume was computed by truncating the closer (or lower redshift) volumes, since this method included only the solid angle of the furthest frame. Successive “snapshot” files were written at double the light-crossing time for the simulation volume. Hence, successive frames are quite close in their corresponding redshifts. We typically have redshift slices spaced by  $\sim 8$ – $15$  Myr in cosmic time. Single time-slices were chosen for the redshift bins for  $z \leq 6.3$ , and 5 time-slices were combined, or “stacked”, for  $z > 6.3$  to keep the resulting database manageable.

#### 3.2. Interface to the BC03 models

The simulation output binary-files were read, and new files written from these data for the star-particles, including model age and metallicity. The age of the star-particle was determined by when it was formed relative to the cosmic time of the model output. The cosmic age of the output data was computed from the redshift of the time-slice, according to the  $\Lambda$ CDM model assumed, although the value of  $\Omega_\Lambda$  was updated to 0.73 to reflect more recent data, as explained earlier. The metallicity and age were used to map to the appropriate stellar population model and SED in BC03, using the Chabrier (2003) IMF models. We chose the 150 nm restframe region for comparison with the observations in Hathi et al. (2010). These SEDs were redshifted to the (virtual) observer’s rest-frame, and convolved with a filter response function, then multiplied by a simulated telescope aperture and exposure time. These were recorded in a file, along with particle comoving coordinates and model age and metallicity data.

Filters were chosen to conform to the criteria in Dahlen et al. (2007). This required that the redshifted 150nm emitted-wavelength lie between the 25th and 75th percentiles of the filter’s response function. Filters  $i$  and  $z$  (Gunn),  $J$  (Johnson), and  $H$  (Bessel and Brett) were taken from the available filters in the BC03 filter file, but the F105W filter from HST WFC3 was added to the file (i.e., Windhorst et al. 2011, Koekemoer et al. 2011).

The integrated flux from the BC03 models was multiplied by the star-particle mass in  $M_\odot$ , and converted to ergs/sec. The energy density per unit wavelength in the observer’s frame was reduced by a factor  $(1 + z)$  due to the redshift, representing the “k-correction” (Hogg et

<sup>2</sup> <http://www.stsci.edu/jwst/instruments/nircam/operations#imaging>

al. 2002). The flux per unit wavelength was then computed according to the inverse square of the luminosity distance. Note that we are computing the bandpass energy of a single star-particle, not the bolometric magnitude nor its surface brightness, which would include an extra factor of  $(1+z)$ . This is essentially justified by the fact that star-particles are point sources at the HST and JWST telescope resolution, as explained in §3.1. While the initial exposure value was set high to extract as much detail as possible from the model output, it was later reduced by an appropriate factor to take the actual zodiacal background and more realistic exposure times into account. This enabled us to estimate the effect of the sky-background on the simulated “observation.” For example, for a JWST-class instrument of total collecting aperture  $A = 25 \text{ m}^2$ , the exposure time was approximately 11 months for the baseline case when *no* noise was added. When the standard zodiacal noise for L2 was added, corresponding to  $H \approx 22.6 \text{ AB-mag arcsec}^{-2}$  (Windhorst et al. 2011), the exposures were reduced by a factor of  $\approx 70 - 130$ , depending on the effective width (in Hz) of the simulated filter, since the same sky-noise mask with a Poissonian distribution was used to create all the images with sky-background added. This corresponds to more realistic exposure times of  $\approx 2.5 - 4.5$  days for JWST deep fields.

In an actual CCD, or near-IR detector, incoming photons are converted to electrons, which are then counted. To mimic this, the integrated flux was converted to ergs, and divided by  $10^{-12}$ , approximately the energy (‘work function’), needed to produce an electron. Since the intent was not to simulate exactly any particular instrument, the exact factors are unimportant here, provided that the flux and pixel scales are consistent with the values used in introducing the sky-background noise, and approximate the sensitivity of the simulated instrument class. While actual CCDs or IR-detectors have other sources of noise such as read-noise and dark current, these are considered second order effects and are ignored here. For example, dark current is 10-20 times below zodiacal light levels, according to the WFC3 instrument handbook<sup>3</sup>. While read-noise can be significant for very faint observations, in the rest-frame UV we can ignore it for most cases if care is taken regarding the length and number of exposures, which would be done in an actual observation, also according to the WFC3 instrument handbook for the IR detector. The object source also contributes a noise equal to the square root of the source signal due to random effects. This can be reduced by very long exposures, which we simulate here, so this effect is also ignored, as it is also a second order effect. However, this noise is effectively considered when estimating the bin count error for the chi-square fit of the simulated LF to a Schechter function (§4).

This integrated flux gave a simulated ‘electron count’  $N_e$ , where  $F$  is the total integrated object flux, and the telescope aperture is given by the area  $A$ , for an exposure time ( $t$ ):

$$N_e \simeq A t F / 10^{-12} \text{ ergs} \quad (1)$$

where the incident flux  $F_{BP}$  observed through a filter

with bandpass BP, is given by:

$$F_{BP} = \int F_\lambda(\lambda/(1+z), t(z)) R(\lambda) (1+z)^{-1} d\lambda \quad (2)$$

where  $F_\lambda(\lambda)$  is the incident flux and  $R(\lambda)$  is the filter response function. Note that, while the flux calculation is done in the wavelength domain, the computation of AB magnitudes from fluxes in ergs/cm<sup>2</sup>/sec are done in the frequency domain (Oke & Gunn 1983).

When trying to exactly simulate an actual instrument, an optical telescope assembly (OTA) term would need to be included for the effects of the telescope throughput, and also a point-spread-function (PSF) term would need to be included to account for the mirror figure and any segmentation. Since no specific instrument is modeled, we simulate the PSF of the WFC3 IR camera on Hubble by approximating its PSF by a Gaussian function, which is convolved with the FITS image before the sky-noise is added – as described below. Since the WFC3 IR camera has a published FWHM of  $\approx 0.15''$  (Windhorst, et al. 2011) for the F160W filter, and our simulated image pixels are  $\simeq 0.1''$ , we use a Gaussian with  $\sigma = 0.65$ . While the PSF is wavelength dependent and would be smaller for shorter wavelengths, this is taken as a worst-case scenario for the lower redshift simulations, since we see no significant effect for this filter. This procedure is then repeated, but applying the dust-extinction model described in section 3.4. The results of both of these are described in section 5.3 and Figs. 4, 5 and 7.

As noted, the space environment is included by adding the proper zodiacal sky-background (Windhorst et al. 2011). Some of the effect of a telescope PSF is accounted for in the SExtractor image filter mask, by distributing the image over several pixels to increase detection sensitivity to faint, low-SB objects. The SExtractor mask used has a FWHM value of 2 pixels, or  $\approx 0.2''$  for the image scale used here.

### 3.3. Simulated “Observed” Object Magnitudes

To compute the “observed” apparent magnitude in the AB system, the simulated exposure was converted to a flux per unit frequency. The integrated flux was divided by the artificial aperture and time constants, converting energy units to ergs s<sup>-1</sup>, and dividing by the filter effective width in Hz to obtain  $f_\nu$  in ergs s<sup>-1</sup> cm<sup>-2</sup> Hz<sup>-1</sup>.

The AB magnitude was then obtained using  $m_{AB} = -2.5 \log(f_\nu) - 48.60$  (Oke & Gunn 1983), where  $f_\nu$  is in ergs s<sup>-1</sup> cm<sup>-2</sup> Hz<sup>-1</sup>. To convert to an absolute  $M_{AB}$  magnitude in the rest-frame emitted band, we use  $M_{AB} = m_{AB} - 5 \log(D_L/\text{Mpc}) - 25 + 2.5 \log(1+z)$ , where  $2.5 \log(1+z)$  is the k-correction, which is positive, since magnitudes are computed in the frequency domain (Hogg et al. 2002). In the prior calculation of the total apparent ‘observed’ energy, the calculation was in the wavelength domain, since the SEDs and filter responses were given as functions of  $\lambda(\text{\AA})$ . The calculation of the absolute magnitudes is performed on the photometric catalog as produced by SExtractor when detecting ‘objects’ — clusters of star-forming particles — which are assumed to represent galaxies in formation (see discussion below). We used the parameter PHOT.APERTURES set to 10 (diameter in pixels) in SExtractor, and the de-

<sup>3</sup> [http://www.stsci.edu/hst/HST\\_overview/documents](http://www.stsci.edu/hst/HST_overview/documents)

fault settings of PHOT\_AUTOPARAMS which were 2.5, 3.5. The flux used in the magnitude calculation is from the FLUX\_AUTO field output from SExtractor, which is the flux within a Kron-like elliptical aperture. Such an aperture is appropriate for faint largely unresolved objects.

### 3.4. SExtractor Parameter and Photometry Testing

We experimented with several of the SExtractor parameter settings by creating catalogs with different settings of either the synthetic FITS files from the simulation or creating artificial fits images, explained below. We compared the catalog detection counts and, in some cases, plotted the LF from those catalogs to compare the distribution of those detections with luminosity.

We note that these artificial images represented a different challenge to detection by SExtractor, compared with real galaxy images. In real images of galaxies of at least several pixels in size, the light is spread out over adjacent pixels of the image, until the surface brightness falls below detection limits. Thus, the object is seen as composed of adjacent or contiguous pixels, which is required by SExtractor for detection. However, our images consist of separate “star-particles”, where the light is concentrated in a single pixel. Without dust and an actual instrument PSF to diffuse the light into adjacent pixels, smaller objects may be ‘seen’ by SExtractor to consist of distinct separate pixels. Hence, SExtractor would categorize these as a group of stars, or as several smaller source objects, rather than a single object. For this reason, Gaussian masks were used to diffuse the concentrated sources. This required the testing of different size masks.

We tested different Gaussian masks (“FILTER\_NAME” parameter in the SExtractor configuration file) with Gaussian  $\sigma$  values ranging from 1.5 to 5.0 and mask size from  $3 \times 3$  to  $9 \times 9$  pixels. These were tested against the FITS image from the simulation at redshift 6.01. The LFs were plotted and the results formed two distinct groups. There was negligible difference in the LF at ABmag brighter than  $-14$  mag. Fainter than  $-14$  mag, the Gaussian masks with  $\sigma$  values of 1.5 and 2.0 and size of  $3 \times 3$  pixels showed a sharply reduced number of detections compared with the other masks, being down an order of magnitude at ABmag  $\approx -12$  mag. The mask with  $\sigma = 2.0$  and  $5 \times 5$  generally had the most detections, hence that mask was used for this study, although the differences were small compared with the other masks in that group.

In addition, we ran tests of simulated images with 81 source pixels each given a constant flux-count of  $10^6$ , but spread out over a pattern with a variable spacing over a grid of  $81 \times 81$  pixels in a  $200 \times 200$  pixel frame. All pixels were separated by at least one, and up to 24 background pixels. This was then converted to a FITS file for the simulation testing. This FITS image was scanned with SExtractor using the settings described above *both without* adding a PSF-convolution, and *with* a PSF-convolution using a Gaussian with a FWHM of 0.15” and a Poisson distributed noise-background with a mean count of  $10^4$ . Note that the source was made constant, not random. This was done to facilitate testing the effectiveness and accuracy of the SExtractor photometry, specifically the total Kron aperture-flux recovered from the detected ob-

jects. That is, we could more readily tell if the photometry captured an integer number of source pixels and if the background was not being subtracted correctly. By convolving with the Gaussian PSF, some of the signal was distributed into neighboring pixels. By comparing the SExtractor-calculated photometry of objects for the two different detection schemes, we could judge the amount of source flux that was not captured by SExtractor. It was found that before being convolved with the PSF, SExtractor found 10 objects with a total flux-count of  $4.0 \times 10^7$ . Converting flux units to magnitudes, SExtractor found an average difference of  $0.00004 \pm 0.00009$  mag compared with what would be expected if an integer number of sources were found, before convolving with the PSF. After convolving with the PSF, SExtractor found 29 objects with a total flux count of  $9.37 \times 10^7$ , and an average difference of  $0.003 \pm 0.002$  mag compared with the expected value. This test was repeated with higher background noise levels. With a mean background count of  $10^5$ , before convolving with the PSF, SExtractor found only 5 objects, reflecting the lower S/N, and an average difference of  $0.003 \pm 0.02$  mag compared with the expected value. After convolving with the PSF, SExtractor found 12 objects and an average difference of  $0.02 \pm 0.01$  mag compared with the expected value. When a background with a mean count of  $10^6$  was used, SExtractor found 12 objects with an average difference  $-0.02 \pm 0.01$  mag compared with the expected value.

Finally, we simulated objects closer to the S/N range of the fainter images created in the numerical simulation. A fixed flux was still used, in order to test the SExtractor photometry, but with an integrated flux count of only  $10^4$ , which is in the range of the simulated star-particle fluxes. For example, the simulation at redshift 6.24, before any adjustment to the simulated exposure time, with the simulated WFC3 IR filter, had fluxes ranging from  $3.5 \times 10^2$  to  $3.1 \times 10^6$  with an average flux count of  $8.9 \times 10^4$ . An object detected by SExtractor in the numerical simulation with a flux count of  $1.0 \times 10^6$  was at a simulated apparent AB magnitude of 32.76 mag and an absolute magnitude of  $-14.02$  AB-mag. After the simulated source signal was reduced by a factor of 83 for the expected background noise for that filter, and to simulate a more realistic exposure time, as discussed in §3.2, a source count of  $1.0 \times 10^6$  corresponded to  $m_{AB}$  of 27.60 mag and  $M_{AB} = -19.18$  mag. These data are given to provide a comparison of the artificial test images with the the simulated images.

A much larger number of particles was then simulated, with variable spacing but more densely packed. Also, a random floating point value in the range from  $-1.0$  to  $+1.0$  pixels was added to the X and Y coordinates to each source pixel. A random background with a mean count of  $10^6$  was added and the image was also convolved — before adding noise — with the PSF for comparison. Without the PSF, SExtractor found 18 objects with an average flux count of  $0.72 \times 10^6$  and a difference of  $-0.002 \pm 0.002$  mag compared with the expected value. After the PSF-convolution, SExtractor found 8 objects with an average flux count of  $0.80 \times 10^6$  and a difference of  $-0.002 \pm 0.002$  mag compared with the expected value.

Therefore, we conclude that SExtractor photometry on these types of objects consisting of discrete relatively high S/N sources, shows no significant flux difference,

even after convolving with a PSF. When the S/N ratio is reduced with the smaller samples we see a systematic error, but this may be due to the smaller sample size, since we again see a small difference with the larger samples even with the higher background-level and smaller source pixel flux count. In addition, we found best results for the parameter DETECT\_THRESH of 1.5 sigmas above background for pixel detection, which was the default setting. We also found a DEBLEND\_NTHRESH setting of 64, rather than the default setting of 32, slightly increased the number of detections.

### 3.5. Processing of the Simulated “Observed” Images

The files of flux and sky-projected object coordinates were translated into FITS files using publicly available utilities from the High Energy Astrophysics Science Archive Research Center of NASA <sup>4</sup>. Their size was set by the number of pixels along the sky-projected axes, according to the comoving distance at that redshift and the  $\Lambda$ CDM model used, as described above. The FITS object frame or merged frames were combined with a simulated sky-noise background FITS file. This noise frame was computed using a Poisson distribution. As explained previously, a convolution mask was used in SExtractor to improve the classification of close groupings of star-particles, including normal galaxies and mergers, as extended objects rather than as isolated star-like objects. This was necessary, since gas particles and radiative transfer are not currently incorporated in the simulated images.

Various parameters were used to extract the simulated objects, and inspect the sensitivity of the results to the input parameter selection. This is a difficult problem, since we have two main independent sources of error: the simulation itself and the selection criteria used for SExtractor. A gaussian convolution mask of  $5 \times 5$  pixels with a full width half maximum (FWHM) of 2.0 pixels was used. This enables star-particles which are near each other, but not “touching”, to be detected as part of a “single object” (see Fig. 1). We also set the SExtractor object detection at a minimum of 40 pixels above threshold (DETECT\_MINAREA). This was done to remove any spurious identification of pixel groupings which were actually part of the same object as a collection of smaller objects. At the chosen pixel scale of  $0.099''/\text{pix}$ , our 2.0 pixel or  $\approx 0.2''$  convolution kernel, is larger than both the PSFs of HST ( $0.13''$  FWHM) or JWST ( $\approx 0.06''$  FWHM) at  $\approx 1\mu\text{m}$  wavelength, which corresponds to  $\approx 2.2$  kpc convolution kernel, i.e., larger than most SF regions of interest. It is similar to the sizes of faint galaxies expected at these magnitudes (e.g., Windhorst et al. 2008).

### 3.6. Dust Extinction

The effect of dust extinction on the LF is modeled by using the relation from Calzetti et al. (2000) between the UV extinction ( $A_{1600}$ ) and the slope  $\beta$  of the UV continuum, and by using the study of the UV continuum  $\beta$  in Finkelstein et al. (2012).

The data from Finkelstein et al. (2012) is modeled both in terms of redshift and luminosity, with interpola-

tions made between their redshift bins, to yield a continuous function across the luminosity range. The extinction is calculated using the median values for  $\beta$  in Finkelstein et al. (2012), and also using a Monte Carlo selection of  $\beta$  over the calculated scatter in their values. The scatter or spread in the Finkelstein et al. (2012)  $\beta$  values is approximated by a normal distribution with a mean value equal to the median value they give, and a standard deviation equal to the square root of the average of the squares of their positive and negative one-sigma values. These are typically  $\sigma_\beta \approx 0.2$ .

Since Finkelstein et al. (2012) caution that their  $\beta$ -values at  $z \geq 8$  are unreliable, we do not use those, and use the results at  $z = 7.0$  for redshifts  $z = 7.16$  and  $7.68$ . As they consider dust extinction rather unimportant for the higher redshifts, we do not apply a dust extinction to the simulated objects at  $z = 10.38$ . The  $\beta$  values in Finkelstein et al. (2012) ranged from  $-1.8$  at redshift 4 to  $-2.68$  at redshift 7. Our simulated  $A_{UV}$  values range from  $0.64$  mag at redshift 4.52 to  $0.006$  mag at redshift 7.68, and 0 at redshift 10.4. See Table 3 for a breakdown of  $A_{UV}$  values and their  $1-\sigma$  errors, by magnitude range and type of simulation.

The results are given in Sections 5.3 and in 5.4 with a PSF added, and do not show a significant difference in the derived faint-end LF slope alpha-values, even though Table 3 shows differences in the  $A_{UV}$  extinction by magnitude. However, there appears to be an effect from dust on the derived  $M^*$  values at the lower ( $z = 4.5$  and  $5.3$ ) redshifts.

We note that some authors (e.g., Jaacks et al. 2012 and Shimizu et al. 2014) adjust the dust extinction values within a given parameter range to obtain the best fit of their simulated LFs with the observed LFs. We take a different approach in order to preserve the predictive nature of our model. This results in number densities per unit volume that are significantly higher than in the literature. If we adjusted our dust extinction per the prescription in Jaacks et al. (2012) based on a range of  $E(B-V)$  values of 0.0 to 0.30, we would have increased our  $A_{UV}$  to 2.33 mag, and come much closer to predicting the observed LFs. They ended up using  $E(B-V) = 0.10$  for redshifts 6 and 7, which resulted in  $A_{UV} = 0.23$  mag, but their choice was based on that value resulting in a better fit of their simulated LFs to observed LFs. We also note that our approach results in a luminosity-dependent extinction function, rather than an overall extinction, so that it could affect the Schechter fit of the LF, but, as discussed later in §5.3, we do not observe any significant trend here.

## 4. SCHECHTER LF FITTING TO THE DERIVED “OBSERVED” LFS

We fit the LF to a Schechter function by minimizing the chi-square value of the sum of the squares of the differences between predicted counts and object counts in magnitude bins, divided by the predicted bin count. A variable bin-size was used to maximize the degrees of freedom, and to ensure a minimum count per bin to improve the reliability of the fit. A maximum bin count was later imposed, to improve the fit stability by reducing the variability of the bin-counts due to ‘bunching’ of data around the bin magnitude limits, as discussed in more detail below. We also performed a best-fit, selected

<sup>4</sup> <http://heasarc.nasa.gov/lheasoft>

**Table 3**  
Simulated  $A_{UV}$  corrections.

Redshift	$M_{AB} \leq -20$	$-20 < M_{AB} \leq -18$	$-18 < M_{AB}$	Comments
4.52	$0.477 \pm 0.131$	$0.612 \pm 0.155$	$0.640 \pm 0.158$	no winds
5.32	$0.352 \pm 0.183$	$0.260 \pm 0.214$	$0.251 \pm 0.234$	no winds
6.01	$0.201 \pm 0.209$	$0.077 \pm 0.144$	$0.021 \pm 0.087$	no winds
6.01	$0.194 \pm 0.209$	$0.077 \pm 0.140$	$0.023 \pm 0.087$	winds
6.24	$0.156 \pm 0.208$	$0.056 \pm 0.134$	$0.019 \pm 0.090$	no winds
6.24	$0.150 \pm 0.207$	$0.058 \pm 0.136$	$0.018 \pm 0.085$	winds
7.16	$0.121 \pm 0.208$	$0.021 \pm 0.093$	$0.014 \pm 0.085$	no winds
7.16	$0.112 \pm 0.198$	$0.022 \pm 0.098$	$0.010 \pm 0.074$	winds
7.68	$0.136 \pm 0.234$	$0.019 \pm 0.092$	$0.012 \pm 0.073$	no winds
7.68	$0.123 \pm 0.216$	$0.017 \pm 0.085$	$0.006 \pm 0.056$	winds
10.38	0	0	0	

Simulated extinction values  $A_{UV}$  using UV continuum slope  $\beta$  values from Finkelstein et al. (2012).  
Comments column indicates whether simulation includes feedback winds or does not.  
For details, see text (§3.6).

over the ‘‘observed’’ data parameter space, which is also discussed below.

The photometric data collected from the SExtractor catalogs were converted to restframe absolute magnitudes. The filters were chosen such that the sampled restframe emission band was approximately 150 nm, in order to allow comparison with the Hubble WFC3 ERS data of Hathi et al. (2010), and references therein. In Hathi et al. (2010), the authors explain that they used the dual image mode of SExtractor, where one set of images was used for detection and another for the photometry. This was due to the use of multiple filters and the use of MULTIDRIZZLE. They used multiple filters to use the drop-out technique to find candidates for different redshift bins. We already know the redshift of the object a priori, so we mimic what they did, by using the single image mode, in a single filter for each redshift that most closely samples restframe 150 nm.

We fit the LF data to a Schechter function in magnitude space of the form:

$$\Phi(M) = 0.4 \ln(10) \phi^* \exp(-10^{[-0.4(M-M^*)]}) \times 10^{[(-0.4)(\alpha+1)(M-M^*)]} \quad (3)$$

where  $M$  is the absolute magnitude, and  $M^*$  is the characteristic magnitude of the Schechter LF.  $\Phi(M)$  is the volume density count of objects of magnitude  $M$ , with  $M^*$ ,  $\alpha$  and the normalization  $\phi^*$  as free parameters. The fit used the chi-square function:

$$\chi^2 = \Sigma[Y_i - y_i(\theta)]^2 / y_i(\theta), \quad (4)$$

where  $Y_i$  are the measured values, and  $y_i(\theta)$  are the expected values for parameters  $\theta$ , which here are  $M^*$ ,  $\alpha$  and  $\phi^*$ , respectively. The expectation function is the Schechter (1976) function. The free parameters are the characteristic magnitude  $M^*$ , where the exponential function ‘breaks’, the slope  $\alpha$  of the faint-end power-law, and the normalization value  $\phi^*$ .

The minimization technique was essentially a brute force calculation over a broad magnitude range of the parameter space ( $-33.9 \leq M_{AB}^* \leq -16.9$  mag with 500 equal steps and  $-2.4 \leq \alpha \leq -1.0$  with 150 steps), calculating the sum of the residuals for each parameter combination. For simulations where the error was very large

and  $\alpha$  was very steep, the range of  $\alpha$  was extended to  $-3.0$  to avoid biasing the error. For each pair of  $M^*$  and  $\alpha$ , a dynamic fitting was used to minimize the chi-square for the normalization parameter  $\phi^*$ . The code ‘zoomed in’ (i.e., took smaller steps) when the chi-square value fell below a specified threshold value, and then exited when the chi-square value exceeded another threshold after reaching a minimum. This method was checked against a non-dynamic, but much slower search. Chi-square contours were drawn for three confidence levels (68%, 90%, and 99%) by adding the appropriate increment (3.50, 6.25, and 11.30, respectively) to the best-fit minimum chi-square value (see e.g., Practical Statistics for Astronomers, Wall & Jenkins 2012). These are the  $\chi^2_3$ (significance) values for the 3-dimensional parameter space  $M^*-\alpha-\phi^*$  for significance = 0.32, 0.10, and 0.01, respectively, although we plot only the projection in the 2-dimensional parameter subspace  $M^* - \alpha$ .

The fits were also performed by varying parts of the simulated parameter space, namely the maximum absolute magnitude. This was necessary, since the LF drops off steeply at faint magnitudes, generally around mag AB  $\approx -16.0$  to  $-17.0$  with minimal sky-noise ( $\approx 40$  ABmag) and at AB  $\approx -18.0$  for a more realistic sky-background in space ( $\approx 22.6\text{AB} - \text{mag}/\text{arcsec}^2$ ). The cutoff magnitude was found by fitting a Schechter function to the data, and repeating the process, making the cutoff magnitude on the faint-end about 0.25 magnitudes fainter. The cutoff was found by finding the maximum magnitude range for which the reduced chi-square fit was equal to, or less than, a factor of  $\sim 2.0$  for all the LF-redshifts for a given test category (i.e., basic simulation, sky-background added, and *with* feedback winds). In most cases, the reduced chi-square was 1.5 or less.

This dropoff or turnover at the faint-end of the ‘‘observed’’ LF is apparently partly due to incompleteness from a combination of the model pixel resolution and the effect of the imposed sky-background noise. We note, however, that a higher resolution simulation ( $\approx 10^3 M_\odot$  mass per particle) also including gas cooling, heating and star-formation by Read et al. (2006) found the smallest building blocks to occur at  $\approx 10^8 M_\odot$  with a stellar mass of  $\approx 10^6 M_\odot$ , which is very close to our effective



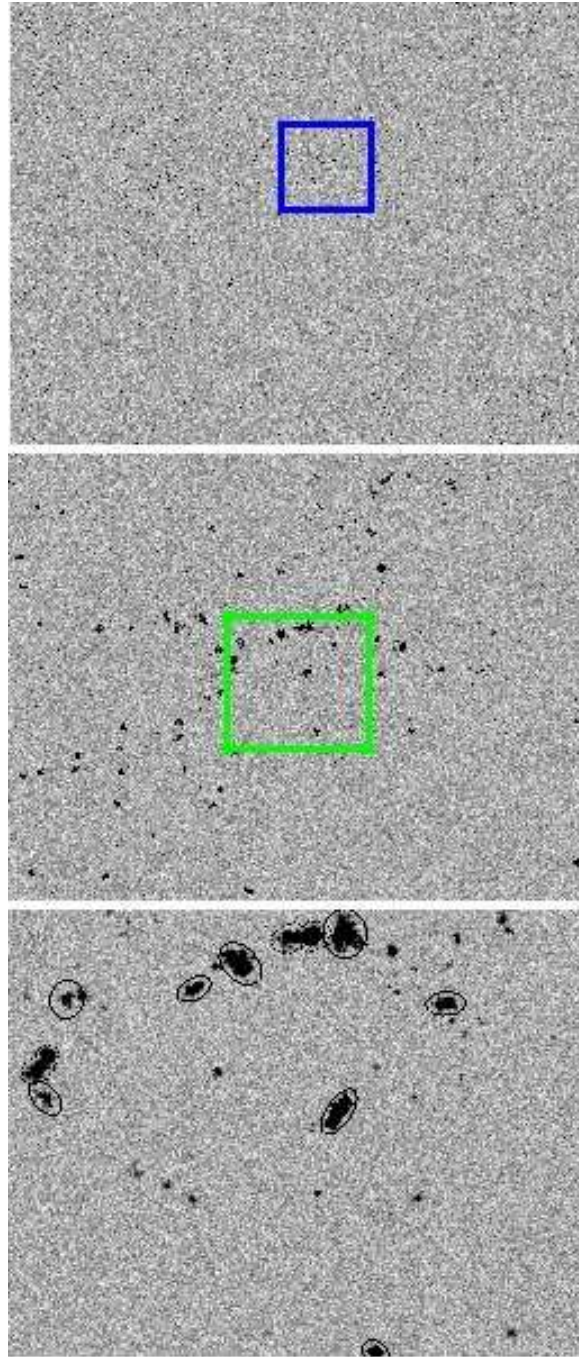


**Figure 1.** FITS file and image aperture file output from SExtractor at redshift  $z = 6.01$  through the simulated WFC3 F105W filter with adopted sky-background  $\approx 22.6 \text{ m}_{\text{AB}} \text{ arcsec}^{-2}$  added to the original simulated image. The image on the top is the entire simulated field  $\approx 110 \text{ arcmin}^2$  in size. The portion in the blue box is enlarged in the middle image,  $\approx 78$  by  $90$  arcsecs. The portion in the green box is shown on the bottom,  $\approx 24.5$  by  $23.4$  arcsecs. Dark pixels are individual ‘star particles’, treated as SSPs (see §2.1). Notice that the images in the contours have luminosity concentrated in the simulated ‘star particle’ pixels and lack the extended surface brightness “wings” of actual observed images.

mass limit. The actual sky-background-induced cutoff was  $\approx 5-6$  magnitudes brighter than the minimum magnitude of the “detected” simulated objects, which were “detected” to  $\approx -10$  to  $-12$  AB-mag with the case of minimal noise-added. This would seem to indicate a preference in the model for forming ‘medium’ sized objects, rather than just a continuation of the power law at the faint-end. This is discussed in more detail later (§6).

Each bin’s effective absolute magnitude was given by the average over the absolute magnitudes for each “detected” object in that bin. To increase the reliability of the chi-square fit, a minimum of 5 objects were required for each bin with a minimum bin size of 0.1 magnitude. To improve the stability of the chi-square fit over the faint-end magnitude range, a variable sized magnitude bin was used. This was achieved by imposing a maximum limit on the number of objects per bin, which reduced the variability of the chi-square value, and improved the consistency of the cut-off magnitude for the best-fits for the different redshift samples. Generally, about 1% of the total number of objects detected by SExtractor was used as the maximum bin-count limit, varying from 60 to a minimum of 15. Trials were used with a range of maximum counts to determine the most stable fit, resulting in approximately twice the number of bins as when the minimum bin size of 0.1 magnitude was used. Thus, the degrees of freedom were also increased, contributing to better chi-square fits in this case.

The uncertainty for each parameter  $M^*$  and  $\alpha$  was found by projecting the 1-sigma contour orthogonally onto each parameter axis. In practice, this amounted to a search in the  $M^* - \alpha$  parameter space for chi-square values bracketing the one sigma (68%) values described above. Chi-square values computed in the search were captured in an array of minimal chi-square values for each  $M^*, \alpha$  pair. The minimum was found by searching over  $\phi^*$  – the LF normalization factor. The LFs and best-fit Schechter functions are shown in figures 2 – 7, both *with* and *without* added zodiacal background noise, and also, *with* additional feedback physics. Confidence contours for the Schechter function parameters  $M^*$  and  $\alpha$  for the fits are also shown.

## 5. LF RESULTS: SIMULATED FAINT-END LF SLOPE EVOLUTION

We examine the results of the numerical simulation:

- *without* feedback in the form of winds (§5.1), and
- *with* feedback (§5.3).
- with adding simulated sky noise from the zodiacal background to the mock images created from the output of the simulations (§5.2 & 5.4).

LFs were fitted to the “observed” images from the simulations with restframe emission at 150 nm (UV) at redshifts in the range of  $z \simeq 4.5$  to 10.4, as shown in Figs. 2 – 7. In Fig. 8 we compare our simulated LFs with more recent observed LFs from Finkelstein et al. (2014) at redshifts 6 to 8. In figures 9 – 11 we show the evolution of the best-fit faint-end LF-slope  $\alpha$  as a function of redshift and compare with the observations (Hathi et al. 2010) and references therein. For a summary of the results, see Table 4.

### 5.1. Simulated Faint-End LF Slope – No Feedback, No Sky-Noise

We first look at the LF fits to the simulation results without feedback ‘winds’ and with extremely low sky-background (Fig. 2), where a minimal amount of sky-noise is added only for SExtractor functionality (e.g., Tamura et al. 2009). In Fig. 9, we compare the redshift evolution of  $\alpha$  from our ‘no-winds’ model results to the observations from Hathi et al. (2010). We find very similar results to the observed Hathi et al. (2010) fits for the faint-end slope  $\alpha$  of the LFs, who found a faint-end slope in the range of  $\alpha \approx -1.2$  to  $-1.8$ , with a redshift dependence of:

$$\alpha = -1.10 - 0.10 z \quad [\text{observed}] \quad (5)$$

Our results for the initial ‘no-winds’ model over the redshift range of  $z \simeq 4.5$  to 7.7, are (Fig. 9):

$$\alpha = -1.00 \pm 0.14 - (0.13 \pm 0.02) z \quad (6)$$

[Simulated – No Winds]

There appears to be some evidence of a lessening of the  $\alpha$ -redshift dependence at higher redshifts, as seen in Figs. 10 & 11. For redshifts  $6.0 \leq z \leq 10.4$ , we find:

$$\alpha = -1.44 \pm 0.19 - (0.06 \pm 0.03) z \quad (7)$$

[Simulated – No Winds]

This is discussed in more detail later, when we discuss the simulations that include feedback in the form of ‘winds’ in the model.

The derived or implied characteristic magnitude,  $M^*$ , does not appear to correspond well with the actual observations (Hathi et al. 2010, Bouwens et al. 2011, 2014). However, we note that this value is generally outside of — or near the boundary of — the bright-end of the magnitude range of the simulated data, as seen in Fig. 2, and also Figs. 3 — 7. Therefore,  $M^*$  may just be an indication of where the bright-end LF ends due to the lack of dynamic range in the simulated data, caused by the limited simulation volume as necessitated by the available computer resources.

Thus, it is likely that  $M^*$  and its evolution is not reliably treated by the simulated data thus far, and that any apparent dependence of  $M^*$  on redshift is mainly due to the changes in the available simulated magnitude interval with redshift. Also, we note that there are increased numbers of detected objects at brighter magnitudes as the redshift decreases, likely due to merger activity developing larger, and hence generally brighter, objects.

We see that the number densities per volume are an order of magnitude or more greater than observed (e.g., Hathi et al. 2010, Bouwens et al. 2011). In following sections, we apply dust extinction and feedback in the form of “winds” to attempt to reduce this overproduction. This overproduction is a common problem in numerical simulations without feedback, usually characterized as an “overcooling” problem (SH03).

### 5.2. The Case of Sky-Background - Without ‘Winds’

In order to compare the model results with more realistic space-based observations, it is necessary to introduce sky-noise (the Zodiacal sky-background) into the

**Table 4**  
Simulated faint-end LF slope  $\alpha(z)$ .

Model Description	$4.5 \leq z \leq 7.7$	$6.0 \leq z \leq 10.4$
No Sky-BG, PSF or Winds	$-1.00 \pm 0.14 - (0.13 \pm 0.02) z$	$-1.44 \pm 0.19 - (0.06 \pm 0.03) z$
With Sky-BG No PSF, Dust, or Winds	$-1.17 \pm 0.20 - (0.10 \pm 0.03) z$	$-1.56 \pm 0.28 - (0.04 \pm 0.04) z$
With Sky-BG & Dust No PSF or Winds	$-1.15 \pm 0.23 - (0.11 \pm 0.03) z$	$-1.80 \pm 0.28 - (0.02 \pm 0.04) z$
With Sky-BG & Dust & PSF, No Winds	$-1.16 \pm 0.22 - (0.12 \pm 0.03) z$	$-1.79 \pm 0.27 - (0.03 \pm 0.04) z$
With Winds, No PSF, Sky-BG, or Dust	N/A	$-1.54 \pm 0.25 - (0.06 \pm 0.04) z$
With Winds, Sky-BG, PSF & Dust	N/A	$-1.84 \pm 0.44 - (0.04 \pm 0.07) z$

The faint-end LF slope  $\alpha(z)$  from best-fit Schechter functions fitted to the model outputs from the basic no feedback winds model and the model including feedback winds. Variations are also shown for adding zodiacal sky-background, a simulated PSF of  $\approx 0.15''$  FWHM and simulated dust extinction (Table 3). Note the agreement in  $\alpha(z)$  evolution – the coefficient of  $z$  – in the redshift range  $4.5 \leq z \leq 7.7$ , and the closeness to the observed  $\alpha(z)$  evolution from Hathi et al. (2010), who found  $\alpha = -1.10 - 0.10 z$ . Note, also, the agreement, within  $1\text{-}\sigma$ , in the  $z$ -coefficient over the redshift range  $6.0 \leq z \leq 10.4$ , and that it suggests a shallower evolution than the lower redshift range.

For details, see §5.

images. This is shown in Fig. 3. As previously discussed, this was done by adding a randomly generated noise frame to the previously generated FITS images from the ‘no winds’ simulation, by carefully adjusting the data-signal levels to achieve the appropriate background level of  $\approx 22.6$  AB-mag arcsec $^{-2}$  at the near-IR ‘detection’ wavelength of  $1.6 \mu\text{m}$  (H-band). While this has the expected effect of truncating the LF at about  $M_{AB} \simeq -18$  mag, we now obtain over the redshift range  $4.5 \leq z \leq 7.7$  (Fig. 10):

$$\alpha = -1.17 \pm 0.20 - (0.10 \pm 0.03) z \quad (8)$$

[Simulated – No Winds, With Sky background]

which is slightly steeper than the results observed by Hathi et al. (2010), but is in agreement with respect to the evolution of  $\alpha(z)$ .

We note that the  $1\text{-}\sigma$  error at  $z = 10.38$  has increased substantially over the *no sky background* case, apparently due to incompleteness effects induced by the added sky-background. This is also reflected in the error contour maps for  $\alpha - M^*$ , which may indicate that more sophisticated fitting methods than chi-square minimization might be needed.

This result compares with the best-fit faint-end slope  $\alpha$  over the higher redshift range of  $6.0 < z < 10.4$ :

$$\alpha(z) = -1.56 \pm 0.28 - (0.04 \pm 0.04) z \quad (9)$$

[Simulated – No Winds – With Sky background]

We observe that the evolution of  $\alpha(z)$  with redshift has become flatter in the higher redshift range in our simulated data when compared to Eq.(8).

We note that  $M^*$  is essentially unaffected by the addition of sky-background — except that, as noted above — the error in the fit is increased due to faint-end incompleteness effects induced by the sky-background. Comparing the counts of detected objects in the samples at different redshifts *with* and *without* sky-background added enables us to estimate completeness of the sky-background samples (Table 2). Since the simulations essentially sample star-particles of  $2.7 \times 10^5 h^{-1} M_\odot$  or  $M$

$\leq -12$  mag (see Fig. 2), while the actual data (sky background) limits the LF to be sampled to  $M \leq -18$  mag (see Figs. 3 — 7), the ratio of the two (Table 2) helps us to assess the incompleteness of the ‘real world’ samples at  $M \geq -18$  mag.

### 5.3. The Case of Dust Extinction and PSF - Without ‘Winds’

The effects of dust extinction, described in §3.5, were added to the catalogs of objects selected by SExtractor from the simulated images with sky-background added (Fig. 4). Later, we also show the effects of adding a simulated PSF to the synthesized images (Fig. 5). The resulting LFs were fitted to a Schechter function and best-fit parameters derived as before, with a limiting absolute AB magnitude  $M_{AB} \approx -18.5$ . We obtain over the redshift range  $4.5 \leq z \leq 7.7$  (Fig. 10):

$$\alpha = -1.15 \pm 0.23 - (0.11 \pm 0.03) z \quad (10)$$

[Simulated – No Winds, With Sky-BG and Dust]

We observe that this result is very similar to Eq.(8), indicating that the addition of dust extinction has not significantly affected our results. This result compares with the best-fit faint-end slope  $\alpha$  over the higher redshift range of  $6.0 \leq z \leq 10.4$ :

$$\alpha = -1.80 \pm 0.28 - (0.02 \pm 0.04) z \quad (11)$$

[Simulated – No Winds, With Sky-BG and Dust]

When a simulated PSF of  $\approx 0.15''$  FWHM is added to the images — before adding sky-background — and then the resulting catalog has dust extinction applied, we obtain — over the redshift range  $4.5 \leq z \leq 7.7$ :

$$\alpha = -1.16 \pm 0.22 - (0.12 \pm 0.03) z \quad (12)$$

[Simulated – No Winds, With Sky-BG, Dust and PSF]

Again, we note the similarity of this result to Eqs.(8) and (10), indicating that the addition of the simulated PSF makes little difference to our results, likely due to the nature of our simulated images and the use of the Gaussian filter in SExtractor, as discussed previously.

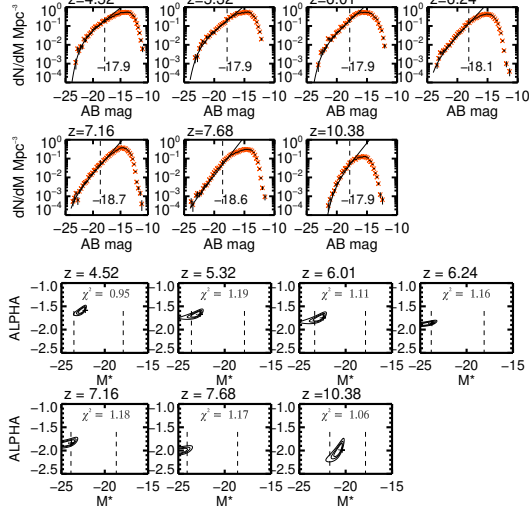


**Figure 2.** The Luminosity Function  $dN/dM/Mpc^3$  vs. AB-mag of simulations *without feedback winds* and the confidence-region panels of the best-fit Schechter functions in the  $\alpha$ - $M^*$  parameter space. The contours indicate 68%, 90%, and 99% confidence levels. The best-fit Schechter functions are given by the solid black curves in the upper panels. These are from images created *without adding sky-background noise*. The LFs are at numerically simulated redshifts of 4.5, 5.3, 6.01, 6.24, 7.16, 7.68, and 10.38. The vertical dotted lines in the upper LF plots indicate the faint-magnitude cutoffs used, when obtaining a chi-square fit to the Schechter function with a reduced chi-square value of no more than 1.2, and an absolute magnitude brighter than  $M_{AB} \simeq -17.5$  mag.

This result compares with the best-fit faint-end slope  $\alpha$  over the higher redshift range of  $6.0 \leq z \leq 10.4$ :

$$\alpha = -1.79 \pm 0.27 - (0.03 \pm 0.04) z \quad (13)$$

[Simulated – No Winds, With Sky-BG, Dust and PSF]

We note that these compare very closely to the prior results without UV dust extinction and without the PSF applied to the images before SExtractor. This is because the median faint galaxy size is somewhat larger than the PSF\_FWHM, so that convolving with the PSF does not make a huge difference, other than perhaps a slight loss in sensitivity.

#### 5.4. Effects on faint-end LF slope $\alpha$ from Feedback due to ‘Winds’

In Figs. 6 & 7, we examine the fits of the LFs to a Schechter function with feedback ‘winds’ enabled. A smaller dependence of  $\alpha$  on redshift is now seen in the model results (Figs. 9 & 10) when the ‘winds’ feedback are enabled. We note that these simulations cover only a higher redshift range, due to the limited computing time available for running these more expensive simulations.

We do not get a good fit to the observed data of Hathi et al. (2010) over their observed redshift range (see Fig. 9). However, when comparisons are made over the redshift range  $6.0 < z < 10.4$ , the  $\alpha$ -redshift dependence slope of the ‘no-winds’ and ‘winds’ cases are very similar (Fig. 11). For the best fit Schechter function of the ‘winds’ feedback case over the redshift range  $6.0 < z < 10.4$ , we find:

$$\alpha = -1.54 \pm 0.25 - (0.06 \pm 0.04) z \quad (14)$$

[with Winds and No Sky-background]

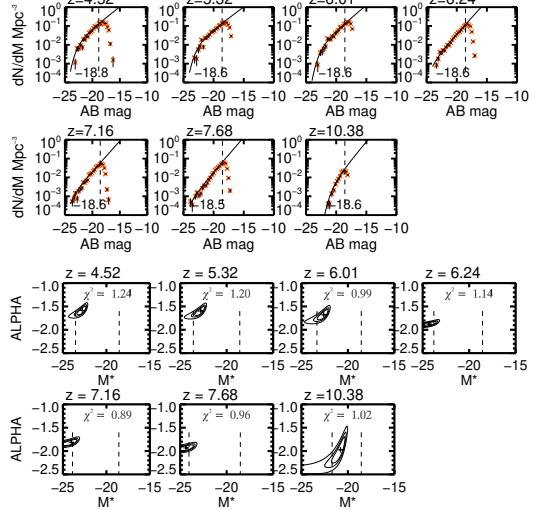


**Figure 3.** The Luminosity Function  $dN/dM/Mpc^3$  vs. AB-mag of simulations *without feedback winds but with added sky-background noise* of  $\approx 22.6$  AB-mag/arcsec<sup>2</sup>. The lower panels are the confidence-region plots of best-fit Schechter functions in the  $\alpha$ - $M^*$  parameter space. The contours indicate 68%, 90%, and 99% confidence levels. They are at numerically simulated redshifts of 4.5, 5.3, 6.01, 6.24, 7.16, 7.68, and 10.38. The vertical dotted lines in the upper LF plots indicate the faint-magnitude cutoffs used when obtaining a chi-square fit to the Schechter function with a reduced chi-square value of no more than 1.25, and  $M_{AB}$  brighter than  $\simeq -18.5$  mag, to exclude the incompleteness region of the LF. Note the effect of the sky-background noise on the incompleteness of the LF, and how this outweighs the non-Schechter turnover in the LF of the simulated data without sky-BG at magnitudes fainter than  $M_{AB} \simeq -17.5$  mag (see Fig. 2).

We note that the slope of this result compares well with the ‘no-winds’ case (Eq.(7)), i.e., the  $\alpha(z)$  curves are parallel, but somewhat displaced in  $\alpha$ -space.

When we add the effects of dust extinction, PSF, and sky-background as described in §5.3 (Fig. 11), we obtain the best-fit of the LFs to a Schechter function over the redshift range  $6.0 < z < 10.4$ :

$$\alpha = -1.84 \pm 0.44 - (0.04 \pm 0.07) z \quad (15)$$

[with Winds, Sky-background, Dust, and PSF]

We note the apparent lessening of the  $\alpha(z)$  dependence alluded to previously. This is not totally unexpected. One would expect a power-law dependence of the faint-end slope  $\alpha \simeq -2$  in the initial galaxy development, due to the primordial power spectrum which predicts  $\alpha \equiv -2$ . As galaxy assembly evolution proceeds, we see a reduction in the steepness of  $\alpha$ , perhaps due to mergers, as modeled by the merger-tree calculations of Khochfar et al. (2007).

We note that Eq.(15) is very close to the ‘no-winds’ simulation of Eq.(11) and (13). At the higher redshift of  $z \approx 10.4$ , we see a slightly more negative value of  $\alpha$ , although these are still close to  $\alpha \simeq -2$ . There is a suggestion of  $\alpha$  leveling out to a range of  $\alpha \simeq -2$  to  $-2.1$ , inspecting the data at redshifts higher than  $z \simeq 7.7$ , although more simulation data points are needed to see a definite trend. Again, this is not unexpected from analytical theory. Also, we note an apparent overall steepening in  $\alpha$  at redshifts  $z > 6$  when the feedback ‘winds’ mechanism is enabled in the simulation. This may be

due to the time delay in star-formation introduced by the winds-feedback in the simulation.

We do not see much of a change in  $M^*$  as a function of  $z$ . Finkelstein et al. (2014, 2015) also found similar results, which they attributed to a lack of dust extinction in high redshift galaxies. Here, as previously described, the feedback from the combined energy of supernovae imparts a velocity to the gas in the model. If the gas resolution could be improved by several orders of magnitude, this may lead to more realistic gas outflows.

To summarize, the winds mechanism — as implemented here — does not seem to affect the evolution of  $M^*$  as much as it seems to affect the  $\alpha$  evolution. Performing additional simulation runs with different ‘winds’ parameter settings — which was limited due to computing time constraints — may help to resolve this issue. Also, a finer resolution, such as ‘zooming’ in on a part of the simulation where star-formation is active, and restarting the simulation from just prior to this would aid in discerning the effect of mass resolution.

Jaacks et al. (2012) ran different simulations at different mass resolution scales and simulation cube sizes to cover the bright, medium and faint-end of the LF scale. Our simulation volume lies between their medium and faint-end simulations. We are close to their mass resolution at the faint-end, where they had gas particles of mass  $1.91 \times 10^5 h^{-1} M_\odot$  since they used only  $2 \times 400^3$  particles. However, for their bright-end they used  $2 \times 600^3$  particles of DM and gas in a simulation box size of  $100 h^{-1}$  Mpc. This results in a volume nearly 200 times larger than ours, permitting them to detect objects two orders of magnitude rarer than in our simulation which enabled them to explore the bright-end better. Jaacks et al. (2012) also reported problems with the break at the bright-end which is discussed more in §6.

We note that over the range of the model parameters and the physics modeled, similar slopes are seen in the  $\alpha - z$  parameter space. The faint-end LF slope  $\alpha$  is seen to become steeper with increasing redshift, and in some cases, parallel tracks somewhat offset in  $\alpha$  are seen. So, the effect of winds seems to be to overall steepen the  $\alpha$ - $z$  relation drastically.

We also note that, while improved somewhat, we still see an excess of objects compared with the observations. This is discussed more in §6.

### 5.5. Comparison of the Simulated LFs with Observation

The simulated LFs at redshifts 6.01, 7.16, and 7.68 are compared to the observed redshifts at 6, 7, and 8 LFs from Finkelstein et al. (2014) in Fig. 8. Since Finkelstein et al. (2014) did not have an LF at redshift 10, we include the simulated redshift 10.38 LF with the redshift 8 observed LF. It will be noted that our volume densities are well in excess of the Finkelstein et al. (2014) densities, except for the simulated redshift 10.38. We have previously discussed that this is, in part due to our not selecting the dust extinction which *creates a best fit* of the simulated LF to observed LFs. We include in the plots the effect of choosing an  $E(B-V)=0.30$  on the Schechter fit, as given by the red curves in Fig. 8. We also show the error curves for the Schechter function best-fits to the observed LFs. We see that increased extinction

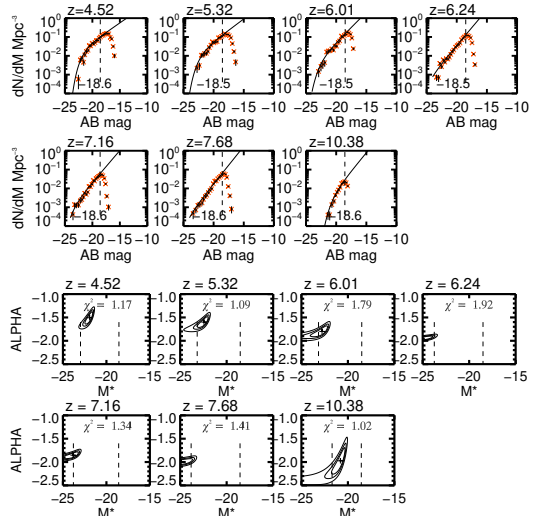


**Figure 4.** The Luminosity Function  $dN/dM/Mpc^3$  vs. AB-mag of simulations *without feedback winds but with added sky-background noise and with UV dust extinction*. The lower panels are the confidence-region plots of best-fit Schechter functions in the  $\alpha - M^*$  parameter space. The contours indicate 68%, 90%, and 99% confidence levels. They are at numerically simulated redshifts of 4.5, 5.3, 6.01, 6.24, 7.16, 7.68, and 10.38. The vertical dotted lines in the upper LF plots indicate the faint-magnitude cutoffs used when obtaining a chi-square best-fit at luminosities brighter than  $M_{AB} \simeq -18.5$  mag, as in the preceding plots.

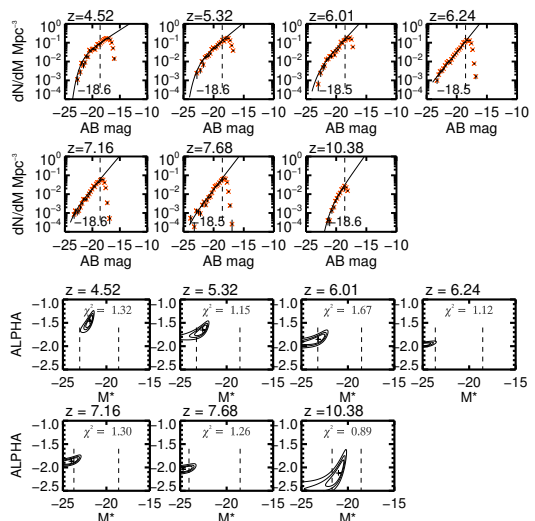


**Figure 5.** The Luminosity Function  $dN/dM/Mpc^3$  vs. AB-mag of simulations *without feedback winds but with added sky-background noise and with UV dust extinction and convolved with a PSF of 0.15'' FWHM*. The lower panels are the confidence-region plots of the best-fit Schechter functions in the  $\alpha - M^*$  parameter space. The contours indicate 68%, 90%, and 99% confidence levels. They are at numerically simulated redshifts of 4.5, 5.3, 6.01, 6.24, 7.16, 7.68, and 10.38. The vertical dotted lines in the upper LF plots indicate the faint-magnitude cutoffs, used when obtaining a chi-square best-fit at luminosities brighter than  $M_{AB} \simeq -18.5$  mag, as in the preceding plots.

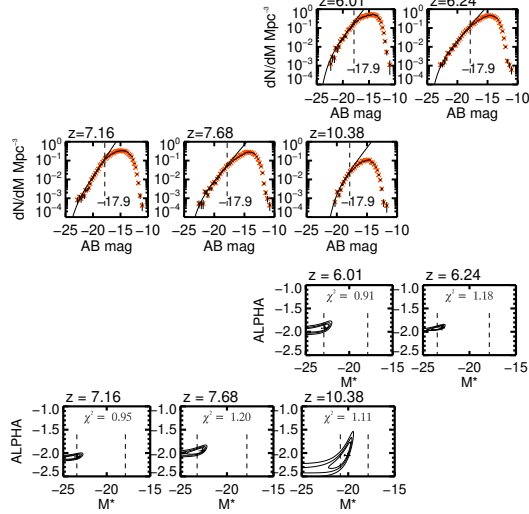


**Figure 6.** The Luminosity Function  $dN/dM/Mpc^3$  vs. AB-mag of simulations *with feedback winds* and confidence-region panels of best-fit Schechter functions in the  $\alpha-M^*$  parameter space. The contours indicate 68%, 90%, and 99% confidence levels. These are from images created without adding sky-background noise. They are at numerically simulated redshifts of 6.01, 6.24, 7.16, 7.68, and 10.38. The vertical dotted lines in the upper LF plots indicate the faint-magnitude cut-offs, used when obtaining chi-square fits to the Schechter function with reduced chi-square value of no more than 1.2, and a luminosity brighter than  $M_{AB} \simeq -17.5$  mag. The missing lower panels are due to the much more expensive simulation, resulting in not being able to continue it to  $z \simeq 4-5$  within the available computing time.

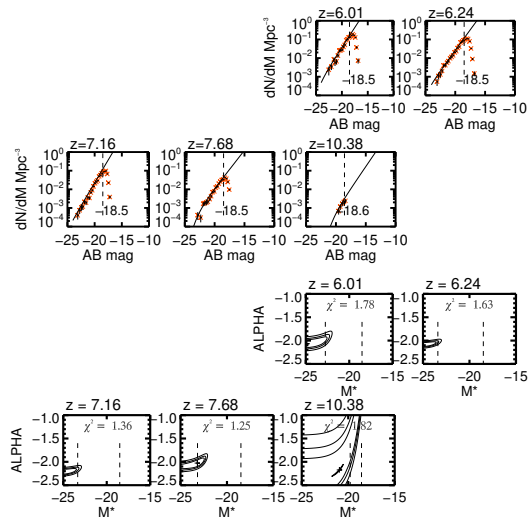


**Figure 7.** The Luminosity Function  $dN/dM/Mpc^3$  vs. AB-mag of simulations *with feedback winds* and *with sky-background, PSF, and dust* and confidence-region panels of the best-fit Schechter functions in the  $\alpha-M^*$  parameter space. The contours indicate 68%, 90%, and 99% confidence levels. These are from images created without adding sky-background noise. They are at numerically simulated redshifts of 6.01, 6.24, 7.16 and 7.68. The vertical dotted lines in the upper LF plots indicate the faint-magnitude cut-offs, used when obtaining a best-fit chi-square fit to the Schechter function with a luminosity brighter than  $M_{AB} \simeq -18.5$  mag.

allows our Schechter fits to be very close to the Schechter fits of the observed LFs, when including the 1- $\sigma$  errors on  $M^*$  and  $\phi^*$  at redshift 7 and within those errors at

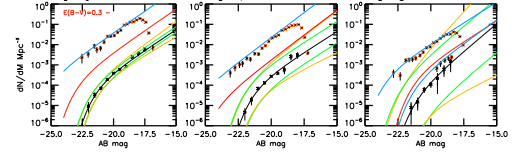


**Figure 8.** The simulated LFs — red x's — vs. the observed LFs — black x's — at redshifts 6, 7, and 8 from Finkelstein et al. (2014). The simulated LFs are *with feedback winds* and *with sky-background, PSF, and dust*. The vertical black bars indicate the error estimates for each magnitude bin. The blue curves indicate the best-fit Schechter functions for the simulated LFs and the black curves indicate the best-fit Schechter functions for the observed LFs. The green curves indicate 1- $\sigma$  errors in  $M^*$  and  $\phi^*$  for the observed LFs and the orange curves including also the 1- $\sigma$  errors in the faint-end slope  $\alpha$  for the observed LFs. The red curves indicate the effects of using a dust extinction on the simulated LF Schechter function best-fit based on an  $E(B-V)=0.3$ . The simulated redshifts are at 6.01, 7.16, 7.68, and 10.38, respectively. Both of the simulated LFs at redshifts 7.68 and 10.38 are included on the rightmost plot with the observed LF at redshift 8. There is no dust extinction for the simulated redshift 10.38.

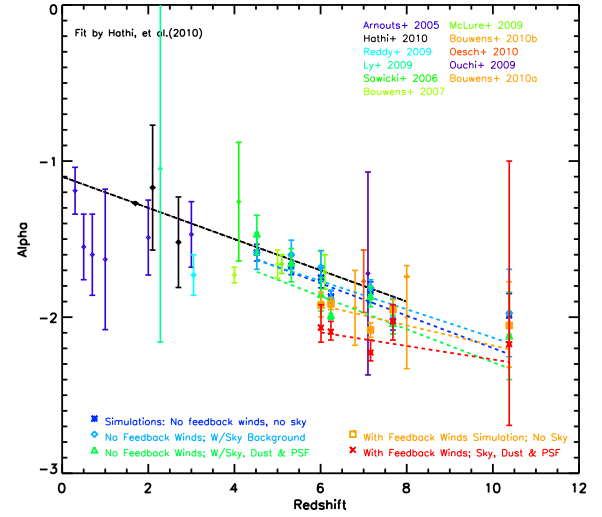


**Figure 9.** The LF faint-end slope  $\alpha$  vs. redshift from Hathi et al. (2010) and references therein, with a best-fit of  $\alpha(z) = -1.10 - 0.10z$ , plus simulations *without* feedback winds and *without* simulated sky-background [Eq.(6)] and *with* simulated sky-background [Eq.(8)]. Also included are simulations *with feedback winds* [Eq. (12)] and with simulated dust absorption and instrumental PSF.

redshift 8.

We also note that — while at very different redshifts — that our simulated LF at redshift 10.38 lies very close to the observed LF at redshift 8. A great increase is seen in the simulated LF density from redshift 10.38 to 7.68, and a gradual increase at lower redshifts. We note that the evolution in the faint-end slope  $\alpha$  of the the LF is similar in our simulated LFs and the observed LFs. Also, our smaller survey volume is seen to affect the ability of the simulation to probe the bright-end of the LF, compared with the observed LFs.

## 6. DISCUSSION

Comparing our results with the observational fits of Hathi, et al. (2010) and references therein to the faint-end LF-slope  $\alpha$  and the evolution of  $\alpha$  with redshift, we find very similar results. However, there appears to be a

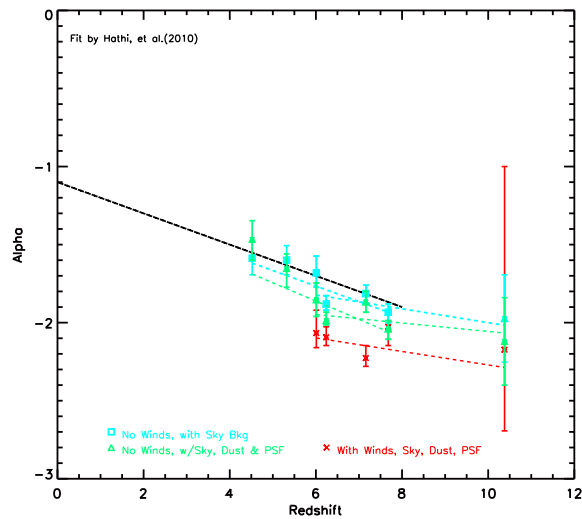


**Figure 10.** The LF faint-end slope  $\alpha$  vs. redshift from Hathi et al. (2010) (Eq. (5)), compared with simulations *without* feedback “winds” and *with* sky-background (Eq. (10) and Eq. (8)), and *with* PSF emulation and *with* simulated dust-extinction, and *with* feedback “winds” over redshift ranges  $4.5 < z < 7.7$  and  $6.0 < z < 10.4$ , using  $\chi^2_3$  statistics (see §5).

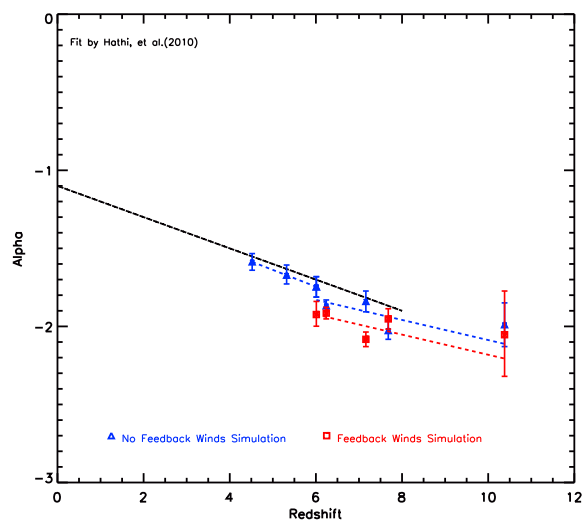


**Figure 11.** The LF faint-end slope  $\alpha$  vs. redshift from Hathi et al. (2010) [Eq. (5)], plus simulations *w/o* and *with* feedback “winds”, fitted over different redshift ranges,  $6 > z > 4.5$  and  $z > 6$  (Eq. (7)) for basic non-feedback simulation, and  $10.4 > z > 6$  for the simulation *with* feedback “winds” case (Eq. (12)), using  $\chi^2_3$  statistics (see §5).

change in the  $\alpha(z)$  dependence at higher redshifts in our simulated data. Salvaterra et al. (2011) found similar results, with their simulated LF faint-end slope having a nearly constant value of  $\alpha = -2.0$  over redshifts 5 — 10.

We note that the characteristic magnitude,  $M^*$ , vs. redshift does not appear to correspond well with the actual observations (e.g., Hathi et al. 2010, Bouwens, et al. 2011). The LF function may be better fit by a power-law than the Schechter function at  $M_{AB} \leq -16$  mag in our simulation results. This was also the conclusion of Bouwens, et al. (2007) and Bowler et al. (2014), regarding similar studies of galaxy formation. However,

our results may be due to limitations on our simulation, discussed below.

As we previously noted, the value of  $M^*$  is generally outside — or near the boundary — of the high-end of the magnitude range in the simulated data. Thus,  $M^*$  may just be an indication of where the best-fit begins to depart from the Schechter function due to the limited simulation volume. Thus, it could be argued that  $M^*$  is not reliably constrained by the currently simulated data, and that any apparent  $M^*$  dependence on redshift is due mainly to the changes in the simulated data magnitude range with redshift. Jaacks et al. (2012) also noted this lack of a distinct break in the bright-end of the LF in their simulations. We note that they used a simulation at the bright-end with a much larger volume (see §5.6), hence the survey volume limitations may well not be the only cause. As noted in other work, simulations with AGN feedback may improve the break at the bright-end of the LF. Closer inspection of our LF curves shows some break at the very bright-end, indicating that even when including basic physics, there appears to be some mechanism for departure of the LF from power-law behavior.

Ultimately, the discrepancy with observed Schechter functions may be due to several reasons. First, the  $M^*$  break in the observations may be largely the result of feedback processes in the real universe, which are lacking in our initial model implementation. In real galaxies, as larger and hence more luminous amounts of gas and stars collect and form in the dark matter potential wells, more of the gas is ejected by feedback mechanisms, limiting the growth of these and in more luminous and massive galaxies also outflows from (weak) AGN. Without these mechanisms, one would just see a continuation of the power-law to brighter fluxes, as seen here. In order to test this, an attempt was made to include feedback in the form of ‘winds’, which was not activated in the earlier model runs. The results of those models are seen in the Figs. 4 and 7, denoted as including ‘winds.’

One interesting feature in the model results is the break in the LF around  $M_{AB} \simeq -18$  mag and the rapid drop-off at fainter magnitudes (seen in Fig. 2), that occurs even before including sky-background effects. Note, due to sky-background induced incompleteness effects, that this feature is not seen — or only hinted at — in the sky-noise added simulated data in Fig. 3. While this effect may be due to mass-resolution artifacts at the limiting mass of  $\approx 10^6 M_\odot$ , we note that this effect is seen at luminosities two orders of magnitude greater than the limiting magnitude of  $M_{AB} = -12$  to  $-10$  mag, assuming a constant M/L ratio. This same effect may also be seen in the simulations of Jaacks et al. (2012). This is of interest since, while hidden from observation due to the actual sky-background, it could affect hierarchical formation by impacting the number of low-mass objects. This flux regime would be more accessible to future space missions, such as JWST.

We have previously noted that the number densities per unit volume are much higher than observed, which may be due to the current treatment of feedback, which may not be treated with the appropriate resolution at this time. The difficulties of modeling feedback, and its importance to galaxy formation was also discussed by SH03 and others (e.g., Dayal et al. 2014). Since the LF curve plots number density vs. luminosity, a slight

decrease in the luminosity would reduce the discrepancy without altering the faint-end LF slope, which can be achieved by including the effects of dust extinction. In fact, as was described in §3.6, some authors (e.g., Jaacks et al. 2012 and Shimizu et al. 2014) selected their dust extinction values on the basis of achieving the best-fit to their LF to observed values. We note that if we increase the dust extinction by several mags we can much improve the fit of our number densities to observed values.

While our initial objective was to study the LF faint-end, in order to explore the bright-end of the LF better — and better simulate the characteristic magnitude  $M^*$  — we need to increase the simulation volume to include more luminous and therefore more rare objects. One way would be to run different volume and mass resolution simulations as in Jaacks et al. (2012) and combine them, as discussed in §5.4. Another way would be to run an initial simulation at lower resolution, but a larger volume, and detect and model those objects of interest over this larger volume only, but at higher resolution.

## 7. SUMMARY

We have predicted the high-redshift galaxy UV LF using galaxy catalogs created by SExtractor from images derived from SSPs derived from a cosmological hydrodynamic simulation, with star-formation modeled via BC03 SSP SED models. We also added the Zodiacal sky-background and additional feedback ‘winds’ physics to investigate their effect on the UV LF.

We find close agreement with observed results (Hathi et al. 2010) for the faint-end slope  $\alpha$  of the UV LF derived from our models. We find little impact from considering winds and sky-background on these observed results over a redshift range from  $z \simeq 4.5$  to  $z \simeq 10.4$ . That is, including the Zodi sky still predicts the same  $\alpha(z)$  relation to within the errors, but to a brighter  $M_{AB}$  limit. We also see a similar evolution of  $\alpha$  with redshift  $z$ , compared to the observed results (Hathi et al. 2010):  $d\alpha(z)/d(z) \simeq -0.10$ . Over this redshift range, we found  $\alpha$  to increase from  $\alpha \simeq -1.5$  at  $z \simeq 4.5$  to  $\alpha \simeq -2.0$  at  $z \simeq 10.4$ . A slight flattening of the slope  $\alpha(z)$  is seen at redshifts  $z > 6$  without the added sky-background:  $d\alpha(z)/d(z) \simeq -0.06 \pm 0.03$ . With the sky-background included, we find a slightly less steep evolution, but still within the  $1-\sigma$  errors.

The bright end of the luminosity function does not show the characteristic magnitude  $M^*$  reported in observations, though there is a hint of a drop off in the LF density at the bright end, which may be due to the unavoidable volume limitations of the simulation. As discussed in §6, this effect has been reported by others (e.g., Jaacks et al. 2012), who had included large survey volumes in their simulations, hence this volume limitation may not be the only factor. Feedback winds included in the simulation had surprisingly little impact on the LF. This could be a resolution issue. It is worth noting that the winds include a delay in star-formation, which may impact the LF density  $\Phi(M)$ .

We also show the possible effects that observational constraints, such as the Zodiacal background, may have on the ability to observe actual properties of galaxy formation. This is especially seen at the faint-end of the LF, due to incompleteness effects from the added sky-background noise. We find a non-Schechter fit to the lu-

minosity function in the regime fainter than  $M_{AB} \approx -17$  mag in the model without sky-background. This is the regime that is very difficult to access by direct observations. It needs to be investigated further if this is due to some artifact, or lack of certain physics in the model. If this result were confirmed to be real in future simulations, it might have implications for galaxy evolution through mergers, since there would be fewer building blocks at fainter magnitudes than a simple extrapolation of the Schechter law would predict.

We thank James Rhoads, Hwihyun Kim, Seth Cohen, and Rolf Jansen for helpful discussions and comments. We are grateful to the ASU Advanced Computing Center (A2C2) for making available computing time for the simulations. RAW acknowledges support from NASA/JWST Grants NAG5-12460 and NNX14AN10G.

## REFERENCES

- Ade, P. A. R., et al. [Planck Collaboration], “Planck 2015 results. XIII. Cosmological Parameters,” arXiv:1502.01589 [astro-ph.CO]
- Bertin, E., & Arnouts, S. 1996, A&AS, 117, 393
- Black, J. H. 1981, MNRAS, 197, 553
- Blaizot J., Wadadekar Y., Guiderdoni B., Colombi S. T., Bertin E., Bouchet F. R., Devriendt J. E. G., & Hatton, S. 2005, MNRAS, 360, 195
- Bolton, J. S., Haehnelt, 2007, MNRAS, 381, L35
- Bouwens R., Cayon L., & Silk J. 1999, ApJ, 516, 77
- Bouwens, R. J., Illingworth, G. D., & Magee, D. K. 2006, ASPC, 351, 145
- Bouwens, R. J., Illingworth, G. D., Franx, M., & Ford, H. 2007, ApJ, 670, 928
- Bouwens, R. J., Illingworth, G. D., Oesch, P. A., et al. 2011, ApJ, 737, 90
- Bouwens, R. J., Bradley, L., Zitrin, A., et al. 2014, ApJ, 795, 126
- Bowler, R. A. A., Dunlop, J. S., McClure, R. J., McCracken, H. J., Furusawa, H., et al. 2014, arXiv:1411.2976
- Bruzual, G., & Charlot, S. 2003, MNRAS 344, 1000
- Calzetti, D., Armus, L., Bohlin, R.C., et al. 2000, ApJ, 533, 682
- Chabrier, G. 2003, PASP, 115, 763
- Chilingarian I. V., Di Matteo P., Combes F., Melchior A.-L., Semelin B., et al. 2010, A&A, 518, A61
- Dahlen, T., Mobasher, B., Dickinson, M., Ferguson, H. C., Giavalisco, M., Kretchmer, C., & Ravindrath, S. 2007, ApJ, 654, 172
- Davé, R., Hernquist, L., Katz, N., & Weinberg, D. H. 1999, ApJ, 511, 521
- Dayal, P., Ferrara, A., Dunlop, J. S., & Pacucci, F., 2014, MNRAS 445, 2545
- Katz, N., Weinberg, D., & Hernquist, L. 1996, ApJS 105, 19
- Finkelstein, S., Papovich, C., Salmon, B, et al., 2012, ApJ, 756, 164
- Finkelstein, S., Ryan, R., Papovich, C., et al., 2014, (submitted to ApJ), arXiv:1410.5439
- Finlator, K., Davé, R., & Oppenheimer, B. D., 2007, MNRAS, 376, 1861
- Gardner, J. P. 2006, IAUS, 1E, 16G
- Gingold, R. A., & Monaghan, J. 1977, MNRAS, 181, 375
- Greisen, E. W., Wells, D. C., & Harten, R. H., 1980, “The FITS Tape Formats — Flexible Image Transport Systems”, Conference on Applications of Digital Image Processing to Astronomy
- Hathi, N., Ryan, R. E. Jr., Cohen, S. H., Yan, H., Windhorst, R. A., et al. 2010, ApJ, 720, 1708
- Haardt, F., Madau, P., 1996, ApJ, 486, 581
- Haas, M. 2010, Ph.D. Thesis, University of Leiden
- Hogg, D. W., et al. 2002, “The K correction”, ArXiv:astro-ph/0210394
- Jaacks, J., Choi, J., Nagamine, K., & Thompson, R. 2012, MNRAS 420, 1606
- Jonsson P., Cox T. J., Primack J. R., & Somerville R. S. 2006, ApJ, 637, 255
- Kochfar, S., Silk, J., Windhorst, R. A., & Ryan, R.E. 2007, ApJL, 668, 115
- Koekemoer, A. M., Faber, S. M., Ferguson, H. C., et al. 2011, ApJS, 197, 36
- Komatsu, E. 2009, ApJS, 180, 330
- Komatsu, E., et al. 2011, ApJS, 192, 18K



- Lotz J. M., Jonsson P., Cox T. J., & Primack J. R. 2008, MNRAS, 391,1137
- Lotz J. M., Jonsson P., Cox T. J., & Primack J. R. 2010, MNRAS, 404,575
- Lucy, L. 1977, AJ, 82, 1013
- Mao, J., Lapi, A., Granato, G. L., de Zotti, G., Danese, L., 2007, ApJ, 667, 655
- Nagamine, K., Cen, R., Furlanetto, S. R., Hernquist, L., Night, C., Ostriker, J., & Ouchi, M., 2006, New Astron. Rev., 50, 29
- Oke, J. B., & Gunn, J. E. 1983, ApJ, 266, 713
- Overzier, R., Lemson, G., Angulo, R. E., Bertin, E., Blaizot, J., Henriques, B. M. B., Marleau, G.-D., & White, S. D. M. 2013, MNRAS, 428, 778
- Read, J. I., Pontzen, A. P., & Viel, M. 2006, MNRAS, 371, 885
- Robertson, B. E., & Bullock, J. S. 2008, ApJL, 685, 27
- Salvaterra, R., Ferrara, A., & Dayal, P., 2011, MNRAS, 414, 847
- Samui, S., Subramanian, K., Srianand, R., 2009, New Astron., 14, 591
- Schaye, J., et al. 2010, MNRAS, 402, 1536
- Schechter, P. 1976, ApJ, 203, 297
- Shimizu, I., Inoue, A. K., Okamoto, T., & Yoshida, N., 2014, MNRAS, 440, 731
- Springel, V. 2000, MNRAS 312, 859
- Springel, V., White S. D. M., Tormen G., & Kauffmann G. 2001, MNRAS, 328,726
- Springel, V., & Hernquist, L. 2002, MNRAS 333, 649
- Springel, V., & Hernquist, L. 2003, MNRAS 339, 289
- Springel, V. 2005, MNRAS 364, 1105
- Stinson, G.S., Brook, C., Macciò, A. V., Wadsley, T. R., & Couchman, H. M. P., 2013, MNRAS, 428, 129
- Tamura, K. 2009, PhD Thesis, Arizona State University
- Thacker, R. J., & Couchman, H. M. P. 2006, International Journal of High Performance Computing and Networking, 4, 303
- Trenti, M., Stiavelli, M., Bouwens, R. J., Oesch, P., Schull, J. M., Illingworth, G. D., et al., 2010, ApJ, 714, L202
- Wall, J. V., & Jenkins, C. R. 2012, Practical Statistics for Astronomers, 2nd Edition, Cambridge University Press
- Windhorst, R. A., Hathi, N. P., Cohen, S. H., Jansen, R. A., Kawata, D., et al. 2011, Advances in Space Research, Volume 41, Issue 12, 1965
- Windhorst, R. A., Cohen, S. H., Hathi, N. P. 2011, ApJS, 193, 27
- Wright 2006, PASP, 118, 1711
- Wuyts, S., et al. 2009, ApJ 700, 799
- Wyithe, J., Stuart B., Yan, H., Windhorst, R. A., & Mao, S. 2011, Nature, 469, 181